PHYSICAL REVIEW B **80**, 195105 (2009)

Imaging properties of lossless double-negative metamaterial wedges: Analytical and numerical investigation

Dimitrios L. Sounas, Nikolaos V. Kantartzis, and Theodoros D. Tsiboukis*
Department of Electrical and Computer Engineering, Aristotle University of Thessaloniki, Thessaloniki GR-54124, Greece

(Received 5 July 2009; published 5 November 2009)

The superlensing characteristics of a lossless double-negative metamaterial wedge are examined in this paper via an analytical technique. The algorithm incorporates the Kontorovich-Lebedev (KL) transform in a mathematically consistent manner whereas the role of the radiation condition on its correct application is quantitatively elucidated. Implementing a ray-approximation algorithm, the proper radiation conditions are resolved and the Helmholtz equation as well as the boundary conditions are accordingly transformed. To this end, the prior formulation introduces a linear operator which, given the KL transform of a specific kind, constructs the corresponding one of a different kind. Thus, the field can be described analytically in the entire domain, showing the ability of the wedge to, perfectly, focus a line source in two points, inside and outside the metamaterial, just like the planar double-negative slab. To validate the proposed analysis, the analytical results are compared to those acquired by means of the finite-difference time-domain method for various geometrical parameters and wedge configurations.

DOI: 10.1103/PhysRevB.80.195105 PACS number(s): 78.20.Ci, 41.20.Jb, 42.15.Dp, 42.30.Wb

I. INTRODUCTION

Double-negative (DNG) metamaterials, a term referring to artificial materials with both constitutive parameters negative,[1] have been in the foreground of the past decade's scientific research, owing to their unique properties, which have been, successfully, exploited in a wide assortment of microwave and optical applications.[2–7] Despite their discrete nature—they are usually implemented as periodic arrangements of miniaturized metallic particles[4,5,8] or networks of lumped circuit elements[2,3]—it is possible to be treated like homogenized bulk entities with frequency-dependent constitutive parameters.[9–12] One of the most intriguing potentials of metamaterials is the realization of imaging devices with resolution below the diffraction limit, as a result of the negative refraction phenomenon and the excitation of surface-plasmon polaritons along the interfaces of double-positive and DNG materials.[13,14] The planar slab constitutes the most representative example of such a superlens and has been shown, both theoretically and numerically,[4,5,15] that it can focus the propagating and part of the evanescent wave spectrum of a point source. In fact, the planar slab obeys to a more general imaging theorem which states that an arbitrary medium is canceled by another one with opposite constitutive parameters.[16] Via this theorem and a coordinates transformation technique it has been proven that the superlensing effect is, also, observed in other nonplanar geometries such as metamaterial spheres or wedges.

Scattering of electromagnetic waves from penetrable wedge-shaped media is a challenging problem of mathematical physics due to the complexity in the extraction of analytical solutions.[17] Apart from numerical approaches,[18] the field can be determined only near the apex of the geometry or under quasistatic assumptions.[19–21] Essentially, the primary hurdle in dealing with such structures rests on the absence of a direct correspondence between field eigensolutions in the diverse domain regions of different wave number, and, therefore, on the difficulty to apply the appropriate boundary conditions to the interfaces of these regions. Exception to this rule is the isorefractive wedge, where the wave number remains the same in the entire domain, and precise analytical solutions may be acquired via the conventional variable-separation technique.[22,23] In the area of metamaterials, an analogous geometry to the isorefractive wedge is the ideal DNG wedge with relative constitutive parameters equal to -1, analyzed in Refs. 24–26 through a variables-separation algorithm. Notice that the importance of examining the ideal DNG wedge lies on its superlensing behavior, which is predicted through the generalized imaging theorem.[16]

In this paper, closed-form expressions for the field of an ideal DNG wedge are extracted via an analytical method based on the Kontorovich-Lebedev (KL) transform. Initially, the imaging characteristics of the structure are investigated by means of a ray-tracing scheme, which explores the power flow in the presence of the metamaterial wedge. The analysis reveals that, if the source lies in a specific angular sector, the power is focused at two points, inside and outside the wedge. Successively, the KL transform is described and its strong association with the radiation condition at infinity is proven. The proposed method consists in transforming both the Helmholtz equation and the proper boundary conditions in the KL domain and, then, returning to the spatial domain via an inverse transform. The radiation condition, which is necessary in the application of the KL transform, is determined from the results of the ray-tracing scheme. Special attention is paid to the case of the source lying in the aforementioned sector, for which outgoing and incoming waves coexist in the same medium, an issue that leads to the definition of an operator that relates KL transforms of different kinds. The analytical results, so obtained, are then compared, in the near-field region, with numerical outcomes from the finite-difference time-domain (FDTD) algorithm[27–29] and a very satisfactory agreement is attained. In essence, the main contribution of the present paper, compared to existing efficient works, is that it provides a complete solution to the ideal

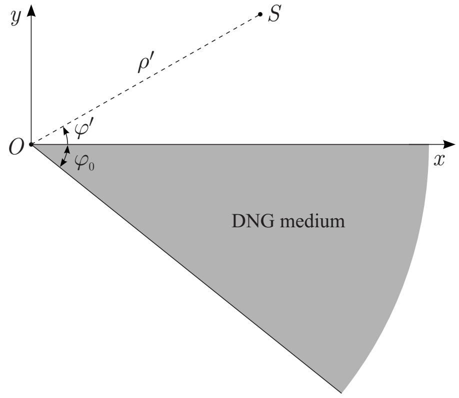

FIG. 1. Geometry of a lossless DNG wedge-shaped medium, illuminated by a point source at S.

DNG wedge problem for an arbitrary position of the source and validates the focusing characteristics of the wedge geometry, predicted, so far, through the generalized imaging theorem. Moreover, a consistent physical interpretation of the derived closed-form expressions, including a comparison with the planar-slab geometry, is supplied, while, all conditions under which the theoretical analysis is applicable to practical geometries, are systematically clarified through the aforementioned numerical verifications.

II. THEORETICAL METHODOLOGY

The geometry under investigation is depicted in Fig. 1, where φ_0 designates the angle of the wedge, ρ', φ' stand for the cylindrical coordinates of the line source which excites the structure, and I_0 is the electric current intensity flowing through the source. Notice that due to the kind of the excitation (i.e., electric current source), and the parallel to the z-axis symmetry of the problem, only transverse magnetic (TM_z) polarized waves evolve. As a consequence, the electric field possesses a single z-directed component, E_z, that depends, solely, on the ρ, φ polar coordinates. Moreover, the DNG medium, occupying the wedge region, is described by the relative constitutive parameters $\epsilon_r = \mu_r = -1$. From a first glance, this specific choice for ϵ_r, μ_r seems nonphysical since DNG materials are always accompanied by dissipation.[30] Nonetheless, taking into account that losses are significant for frequencies near the medium's resonance and that ϵ_r, μ_r become -1 at a frequency far from the resonance, we may assume that losses are small and, as shown in Sec. IV, their effect on the solution can be well predicted. Based on the prior issues and considering an $e^{j\omega t}$ harmonic temporal dependence, E_z satisfies Helmholtz equation,

$$\left(\rho^2 \frac{\partial^2}{\partial \rho^2} + \rho \frac{\partial}{\partial \rho} + \frac{\partial^2}{\partial \varphi^2} + k_0^2 \rho^2\right) E_z(\rho, \varphi) = g(\rho, \varphi), \qquad (1)$$

everywhere in the space of the problem, with $k_0 = \omega\sqrt{\mu_0 \epsilon_0}$, $g(\rho, \varphi) = j\omega\mu_0 I_0 \rho \delta(\rho - \rho')\delta(\varphi - \varphi')$ and $\delta(\cdot)$ representing the Dirac delta function. Furthermore, for the sake of simplicity, throughout this paper we assume that $j\omega\mu_0 I_0 = 1$.

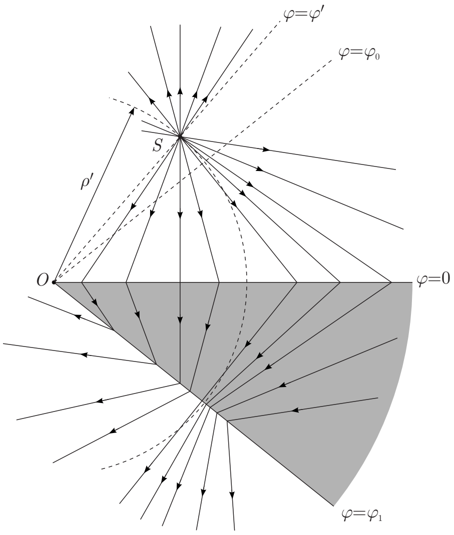

FIG. 2. Ray-approximation diagram for the $\varphi' > \varphi_0$ case.

A. Optical-ray approach

Before proceeding with the mathematical details of the solution, it is deemed instructive to provide a qualitative view of the power flow, via an optical-ray approximation technique. Such an analysis, apart from providing valuable information regarding the physics of the problem, will enable us to determine the appropriate radiation condition that best describes the electromagnetic fields. Bear in mind that this type of condition is essential to guarantee solution uniqueness in Eq. (1) for open-end geometries, such as the class of wedges. In the context of the optical-ray approach, each ray is presumed to originate from the source point (ρ', φ') and undergo a bent at the air-DNG interfaces, according to Snell's law. More specifically, if θ_i, θ_r are the incidence and refraction angles, respectively, measured from the normal vector to the interface in a clockwise sense, it follows that $\theta_r = -\theta_i$. Taking into account this remark, the ray diagram for $\varphi' > \varphi_0$ is drawn in Fig. 2, where, for clarity reasons, $\varphi_1 = 2\pi - \varphi_0$. Note that the rays, initially divergent in the air, converge inside the DNG medium. However, they do not manage to achieve a complete focus before they reach the $\varphi = \varphi_1$ interface, after which they, again, diverge in the air. Additionally, for $\rho > \rho'$, the ρ-directed energy-flow points toward infinity in the air and toward the origin in the metamaterial region.

A rather different behavior is observed for the $\varphi' < \varphi_0$ case, shown in Fig. 3, where $\varphi_2 = 2\pi - \varphi'$ and $\varphi_3 = 2\pi - 2\varphi_0 + \varphi'$. Now, the rays converge as φ varies from 2π to φ_2, thus forming a focus at the (ρ', φ_2) point. As φ decreases further toward φ_1, the rays diverge again, until they reach the second wedge interface. Next, they start converging and form a second focus at the (ρ', φ_3) point while for $\varphi < \varphi_3$ they become divergent, again. As far as the energy is concerned, it flows toward infinity for $0 < \varphi < \varphi_3$, $\varphi_1 < \varphi < \varphi_2$ and toward the wedge apex for $\varphi_3 < \varphi < \varphi_1$, $\varphi_2 < \varphi < 2\pi$. Consequently, the metamaterial wedge with $\epsilon_r = \mu_r = -1$ focuses electromagnetic energy in an analogous manner with the planar slab. In particular, as will be next clarified through a rigorous math-

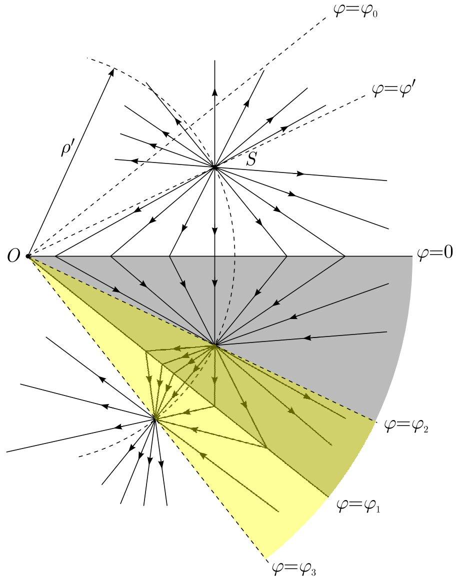

FIG. 3. (Color online) Ray-approximation diagram for the $\varphi' < \varphi_0$ case.

ematical analysis, the field distribution at the focal planes $\varphi=\varphi_2$ and $\varphi=\varphi_3$ is exactly the same as the corresponding one at the source plane $\varphi=\varphi'$, proving that the system possesses an infinite resolution, like the planar geometry.

B. Mathematical formulation

As already stated, among the most important and competent approaches for the manipulation of wedge-scattering problems is the KL transform. Actually, in electromagnetic applications, where a solution of Eq. (1) is pursued, it is mandatory to implement this transform, as proposed in Refs. 31 and 22. Particularly, if $f(x)$ is a function defined over the positive x semiaxis, its KL transform is given through

$$\tilde{f}(\nu) = \text{KL}_i\{f(x)\}(\nu) = \int_0^\infty f(x)H_\nu^{(i)}(kx)x^{-1}dx, \tag{2}$$

with $H_\nu^{(i)}(kx)$ the Hankel function of order ν and kind i, and k a positive real number, which, as will become clear later, represents the wave number of the medium. Then, the inverse KL transform (IKL) receives the form of

$$f(x) = \text{IKL}_i\{\tilde{f}(\nu)\}(x) = -(-1)^i\frac{1}{2}\lim_{\varepsilon\to 0^+}\int_{-j\infty}^{j\infty}\nu e^{\varepsilon\nu^2}J_\nu(kx)\tilde{f}(\nu)d\nu, \tag{3}$$

where $J_\nu(kx)$ stands for the first kind and νth-order Bessel function. Notice that the pair of the KL and its inverse transform, as denoted by Eqs. (2) and (3), is not reciprocal, in the sense that accurate results are ensured, only if the working direction

$$f(x)\xrightarrow{\text{KL}_i}\tilde{f}(\nu)\xrightarrow{\text{IKL}_i}f(x) \tag{4}$$

is followed. Differently speaking, given an $\tilde{f}(\nu)$ function, in order to assure that function $f(x)$, computed via Eq. (3), constitutes the IKL transform of $\tilde{f}(\nu)$, we must, subsequently, obtain the KL transform of $f(x)$ and then prove its equality to $\tilde{f}(\nu)$. It is emphasized that in other integral transforms, such as the Fourier transform, this verification process is unnecessary.

Since E_z fulfills Eq. (1), it is substantial to examine the effects of the KL transform on expressions of the $x^2f''(x)+xf'(x)+k^2x^2f(x)$ form. Therefore, employing definition Eq. (1) and integrating by parts, it can be shown that

$$\begin{aligned}&\text{KL}_i\{x^2f''(x)+xf'(x)+k^2x^2f(x)\}(\nu)\\&\quad=\nu^2\tilde{f}(\nu)+x[f'(x)H_\nu^{(i)}(kx)-kf(x)H_\nu^{(i)\prime}(kx)]\big|_0^\infty.\end{aligned} \tag{5}$$

If the asymptotic behavior of the Hankel function as $kx \to 0^+$ is considered, the second term on the right-hand side of Eq. (5) vanishes at $x=0$. On the contrary, for large kx values, the Hankel function is approximated via

$$H_\nu^{(i)}(kx) \cong \sqrt{\frac{2}{\pi kx}}e^{(-1)^{i+1}j(kx-1/2\nu\pi-1/4\pi)}. \tag{6}$$

Substitution of Eq. (6) into Eq. (5) yields

$$\begin{aligned}&\text{KL}_i\{x^2f''(x)+xf'(x)+k^2x^2f(x)\}(\nu)\\&\quad=\nu^2\tilde{f}(\nu)+\sqrt{\frac{2}{\pi k}}\lim_{x\to\infty}\{\sqrt{x}[f'(x)\\&\qquad+(-1)^ijkf(x)]e^{(-1)^{i+1}j(kx-1/2\nu\pi-1/4\pi)}\},\end{aligned} \tag{7}$$

implying that if

$$\lim_{x\to\infty}\sqrt{x}[f'(x)+(-1)^ijkf(x)]=0, \tag{8}$$

one acquires

$$\text{KL}_i\{x^2f''(x)+xf'(x)+k^2x^2f(x)\}(\nu)=\nu^2\text{KL}_i\{f(x)\}(\nu). \tag{9}$$

A closer inspection of Eq. (8) reveals that, in the case of an $e^{j\omega t}$ harmonic dependence, this formula coincides with the radiation condition for incoming $(i=1)$ or outgoing $(i=2)$ waves in cylindrical coordinates. Consequently, by means of Eq. (9), Eq. (1) transforms to

$$\left(\frac{\partial^2}{\partial\varphi^2}+\nu^2\right)E_z(\nu;\varphi)=\tilde{g}(\nu;\varphi), \tag{10}$$

for $E_z(\nu;\varphi)$ and $\tilde{g}(\nu;\varphi)$ the KL transforms of $E_z(\rho,\varphi)$ and $g(\rho,\varphi)$ with respect to ρ. It is to be stated, herein, that the KL transform kind (i.e., the kind of the Hankel function involved in the transform definition) required to derive Eq. (10) is resolved by Eq. (8). In other words, the radiation condition, which ensures solution uniqueness in field equations, is, implicitly, incorporated in the application of the KL transform. The preceding remark is going to play a critical role in the analysis of the DNG wedge-scattering problem, where, as determined via the optical-ray approach, both incoming and outgoing waves evolve in different regions of the structure.

At this point, it is deemed necessary to provide a physical interpretation of the KL transform, which will contribute to the sounder comprehension of the results in the next sections. Particularly, we are going to investigate the connection of the KL spectrum with propagating/evanescent waves, through the problem of free-space radiation of a line source, located on the x axis ($\varphi'=0$). The obvious presence of solely outgoing waves in this arrangement imposes the use of the second kind of the KL transform so that $\tilde{g}(\nu;\varphi) = H_\nu^{(2)}(k_0\rho')\delta(\varphi)$ in Eq. (10). Then, for the computation of the electric field, Eq. (10) has to be solved along with boundary conditions,

$$\tilde{E}_z|_{\varphi=0} = \tilde{E}_z|_{\varphi=2\pi}, \quad \left.\frac{\partial \tilde{E}_z}{\partial\varphi}\right|_{\varphi=0} = \left.\frac{\partial \tilde{E}_z}{\partial\varphi}\right|_{\varphi=2\pi}, \tag{11}$$

which are derived through the application of the KL transform on field continuity relations,

$$E_z|_{\varphi=0} = E_z|_{\varphi=2\pi}, \quad \left.\frac{\partial E_z}{\partial\varphi}\right|_{\varphi=0} = \left.\frac{\partial E_z}{\partial\varphi}\right|_{\varphi=2\pi}. \tag{12}$$

Passing over the mathematical operations, it follows that

$$\tilde{E}_z(\nu;\varphi) = \frac{H_\nu^{(2)}(k_0\rho')}{2\nu\sin(\nu\pi)}\cos[\nu(\pi-\varphi)], \tag{13}$$

which, in combination with Eq. (3), suggests that the field is expressed as a superposition of $J_\nu(k_0\rho)\cos[\nu(\pi-\varphi)]$ terms, with ν belonging to the imaginary axis. Note that all these terms are solutions of the homogeneous Helmholtz Eq. (1) and, therefore, constitute a complete set of free-space wave functions. If $\mathrm{Im}\{\nu\}\neq 0$, the cosine term in the wave-function expression becomes $\cosh[\mathrm{Im}\{\nu\}(\pi-\varphi)]$, indicating an exponential decay of the amplitude along the φ direction, as we depart from the x axis, where the source is located. Thus, $\mathrm{Im}\{\nu\}\neq 0$ are, primarily, related to the evanescent part of the spectrum, with increasing $|\mathrm{Im}\{\nu\}|$ corresponding to waves deeper in the evanescent region. On the other hand, if $\nu=0$, the field's amplitude remains constant toward the φ direction, implying the connection of this value with propagating waves. It has to be stressed, however, that unlike Cartesian coordinates, there exists no specific ν value, separating evanescent from propagating waves. In fact, propagating and evanescent waves can be detected for every ν, with the former dominating over the latter as $|\mathrm{Im}\{\nu\}|$ grows. Taking into account the prior outcomes, the following sections explore the two principal topologies of the line source excitation in relevance to the wedge and provide analytical expressions for the resulting electromagnetic fields.

III. $\varphi' > \varphi_0$ CASE

After the extraction of the necessary physical interpretations and the development of the relevant mathematical framework, the aforesaid KL-transform-based algorithm is, now, applied to the solution of the wedge-scattering problem. Initiating from the $\varphi' > \varphi_0$ case and revisiting Fig. 2, our space is divided into regions $0<\varphi<\varphi_1$ (region 1) and $\varphi_1 < \varphi < 2\pi$ (region 2), where the energy flows toward infinity and the origin, respectively. More specifically in region 1, the electromagnetic field is expected to exhibit an $e^{-jk_0\rho}/\sqrt{\rho}$ dependence for large ρ, thus imposing the radiation condition

$$\lim_{\rho\to\infty}\sqrt{\rho}\left(\frac{\partial E_{1z}}{\partial\rho} + jk_0E_{1z}\right) = 0, \tag{14}$$

with index 1 referring to the specific region. So, the Helmholtz equation, via the KL transform of the second kind, becomes

$$\left(\frac{\partial^2}{\partial\varphi^2} + \nu^2\right)\tilde{E}_{1z}(\nu;\varphi) = H_\nu^{(2)}(k_0\rho')\delta(\varphi-\varphi'), \tag{15}$$

for $\tilde{E}_{1z}(\nu;\varphi) = \mathrm{KL}_2\{E_{1z}(\rho,\varphi)\}$. Its general solution is

$$\tilde{E}_{1z}(\nu;\varphi) = \frac{H_\nu^{(2)}(k_0\rho')}{2\nu\sin(\nu\pi)}\cos[\nu(\pi-|\varphi-\varphi'|)] + a_1(\nu)\cos(\nu\varphi) + b_1(\nu)\sin(\nu\varphi), \tag{16}$$

where $a_1(\nu), b_1(\nu)$ are functions to be resolved later, through the pertinent field boundary conditions. On the contrary, in region 2, occupied by the metamaterial wedge, there exist incoming waves. Furthermore, since inside a DNG medium the phase advance and the energy-flow directions are opposite, it is deduced that as $\rho\to\infty$, the electric field intensity, $E_{2z}(\rho,\varphi)$, obtains, again, the $e^{-jk_0\rho}/\sqrt{\rho}$ form. In other words, Eq. (14) is, also, valid for $\varphi_1<\varphi<2\pi$ and the second-kind KL transform of $E_{2z}(\rho,\varphi)$ in region 2 satisfies Eq. (15), with its right-hand side, however, equal to zero. Hence,

$$\tilde{E}_{2z}(\nu;\varphi) = a_2(\nu)\cos(\nu\varphi) + b_2(\nu)\sin(\nu\varphi), \tag{17}$$

for $\tilde{E}_{2z}(\nu;\varphi) = \mathrm{KL}_2\{E_{2z}(\rho,\varphi)\}$. The unknown functions $a_2(\nu), b_2(\nu)$, together with $a_1(\nu), b_1(\nu)$, are derived from the continuity of the tangential electric and magnetic field intensity components on the air-DNG interfaces, written as

$$E_{1z}|_{\varphi=0} = E_{2z}|_{\varphi=2\pi}, \quad \left.\frac{\partial E_{1z}}{\partial\varphi}\right|_{\varphi=0} = -\left.\frac{\partial E_{2z}}{\partial\varphi}\right|_{\varphi=2\pi}, \tag{18a}$$

$$E_{1z}|_{\varphi=\varphi_1} = E_{2z}|_{\varphi=\varphi_1}, \quad \left.\frac{\partial E_{1z}}{\partial\varphi}\right|_{\varphi=\varphi_1} = -\left.\frac{\partial E_{2z}}{\partial\varphi}\right|_{\varphi=\varphi_1}. \tag{18b}$$

Applying the second-kind KL transform to Eq. (18),

$$\tilde{E}_{1z}|_{\varphi=0} = \tilde{E}_{2z}|_{\varphi=2\pi}, \quad \left.\frac{\partial \tilde{E}_{1z}}{\partial\varphi}\right|_{\varphi=0} = -\left.\frac{\partial \tilde{E}_{2z}}{\partial\varphi}\right|_{\varphi=2\pi}, \tag{19a}$$

$$\tilde{E}_{1z}|_{\varphi=\varphi_1} = \tilde{E}_{2z}|_{\varphi=\varphi_1}, \quad \left.\frac{\partial \tilde{E}_{1z}}{\partial\varphi}\right|_{\varphi=\varphi_1} = -\left.\frac{\partial \tilde{E}_{2z}}{\partial\varphi}\right|_{\varphi=\varphi_1}. \tag{19b}$$

Then, substitution of Eqs. (16) and (17) into Eq. (19) and solution of the resulting 4×4 linear system of equations, leads to

$$a_1(\nu) = \frac{H_\nu^{(2)}(k_0\rho')}{2\nu\sin(\nu\pi)}\frac{\sin(\nu\varphi_0)}{\sin[\nu(\pi-\varphi_0)]}\cos(\nu\varphi'), \tag{20a}$$

$$b_1(\nu) = \frac{H_\nu^{(2)}(k_0\rho')}{2\nu\sin(\nu\pi)}\frac{\sin(\nu\varphi_0)}{\sin[\nu(\pi-\varphi_0)]}\sin(\nu\varphi'), \qquad (20b)$$

$$a_2(\nu) = \frac{H_\nu^{(2)}(k_0\rho')}{2\nu\sin[\nu(\pi-\varphi_0)]}\cos[\nu(\pi+\varphi_1-\varphi')], \qquad (21a)$$

$$b_2(\nu) = \frac{H_\nu^{(2)}(k_0\rho')}{2\nu\sin[\nu(\pi-\varphi_0)]}\sin[\nu(\pi+\varphi_1-\varphi')]. \qquad (21b)$$

Overall, the KL transform of the electric field intensity in the two regions is given by

$$\tilde{E}_{1z}(\nu;\varphi) = \frac{H_\nu^{(2)}(k_0\rho')}{2\nu}\frac{\cos[\nu(\varphi_0-\pi+|\varphi-\varphi'|)]}{\sin[\nu(\pi-\varphi_0)]}, \qquad (22)$$

$$\tilde{E}_{2z}(\nu;\varphi) = \frac{H_\nu^{(2)}(k_0\rho')}{2\nu}\frac{\cos[\nu(\pi+\varphi_1-\varphi-\varphi')]}{\sin[\nu(\pi-\varphi_0)]}. \qquad (23)$$

Subsequently, our analysis concentrates on the computation of the IKL transforms of Eqs. (22) and (23), where due to their similar extraction stages, only the process for the former is described. Therefore, according to Eq. (3), the electric field intensity in region 1 is expressed as

$$E_{1z}(\rho,\varphi) = -\frac{1}{4}\lim_{\varepsilon\to0^+}\int_{-j\infty}^{j\infty} e^{\varepsilon\nu^2}J_\nu(k_0\rho)H_\nu^{(2)}(k_0\rho') \times\frac{\cos[\nu(\varphi_0-\pi+|\varphi-\varphi'|)]}{\sin[\nu(\pi-\varphi_0)]}d\nu. \qquad (24)$$

The integral on the right-hand side of Eq. (24) can be simplified into an infinite sum through a deformation of its integration path. For this objective, nonetheless, the asymptotic behavior of Bessel and Hankel functions for large-order amplitudes, has to be known. Hence, assuming that $\nu=|\nu|e^{j\psi}$, with $|\nu|\to\infty$, it holds, by means of Ref. 17, that

$$|J_\nu(x)| \sim \frac{1}{\sqrt{2\pi|\nu|}}e^{-|\nu|(\cos\psi\ln 2|\nu|/ex-\psi\sin\psi)}, \qquad (25)$$

$$|H_\nu^{(2)}(x)| \sim \sqrt{\frac{2}{\pi|\nu|}}e^{|\nu|(\cos\psi\ln 2|\nu|/ex-\psi\sin\psi)}, \qquad (26)$$

for $x>0$, $|\psi|<\pi$ in Eq. (25) and $-\pi/2<\psi\leq\pi/2$ in Eq. (26). Now, if $\rho>\rho'$ is supposed, the integration path is deformed along the C curve of Fig. 4, defined by $\nu=|\nu|e^{\pm ja}$ for $\pi/4<a<\pi/2$. Such a deformation is based on the fact that the integrand along the C_1, C_2 arcs, as $|\nu|\to\infty$, is proportional to $e^{|\nu|[|\nu|\varepsilon\cos(2\psi)-w]}/(\pi|\nu|)$, with $w=\cos\psi\ln(\rho'/\rho)-|\varphi_0-\pi+|\varphi-\varphi'||+|\pi-\varphi_0|$. Therefore, the integral vanishes on C_1, C_2. Additionally, the particular integrand does not have any pole singularities inside the closed contour formed by the imaginary axis and the C, C_1, C_2 arcs so leading to

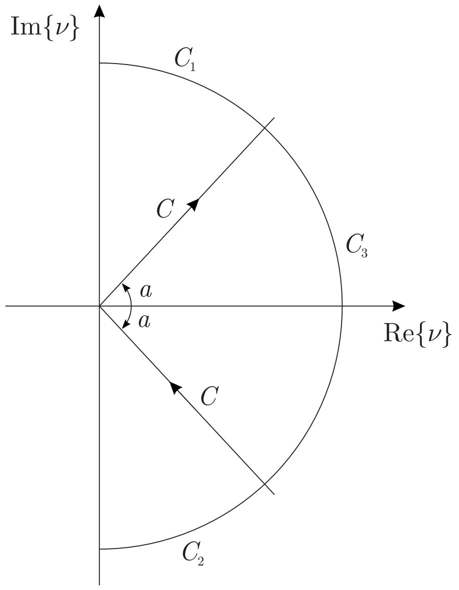

FIG. 4. Deformation of the integration path of the IKL-transform integral.

$$E_{1z}(\rho,\varphi) = -\frac{1}{4}\lim_{\varepsilon\to0^+}\int_C e^{\varepsilon\nu^2}J_\nu(k_0\rho)H_\nu^{(2)}(k_0\rho') \times\frac{\cos[\nu(\varphi_0-\pi+|\varphi-\varphi'|)]}{\sin[\nu(\pi-\varphi_0)]}d\nu. \qquad (27)$$

Observe that the above integral converges even if $\varepsilon=0$, an issue which enables us to neglect the limit and the $e^{\varepsilon\nu^2}$ term. Successively, the C path is closed along the C_3 arc for $-a<\psi<a$, where the integrand for large $|\nu|$ values becomes $e^{-|\nu|w}/(\pi|\nu|)$. It is stressed that since $|\psi|<|a|<\pi/2$ and $\rho'>\rho$, one gets $\cos\psi\ln(\rho'/\rho)>0$. Also, when $|\varphi-\varphi'|\leq|\pi-\varphi_0|$, it stands $|\pi-\varphi_0|-|\pi-\varphi_0-|\varphi-\varphi'||=|\varphi-\varphi'|>0$ while if $|\varphi-\varphi'|>|\pi-\varphi_0|$, which is valid only for $\varphi>\varphi'$, it holds that $|\pi-\varphi_0|-|\pi-\varphi_0-|\varphi-\varphi'||=2\pi-2\varphi_0+\varphi'-\varphi>2\pi-2\varphi_0+\varphi'-\varphi_1=\varphi'-\varphi_0>0$. Conclusively, w is, always, positive and the integral on C_3 vanishes. As a result, the integral in Eq. (27) is equal to the sum of the integrand residues at the poles confined in the closed contour, defined by C and C_3 arcs. Thus, after some algebraic manipulations,

$$E_{1z}(\rho,\varphi) = \frac{j\pi}{2(\pi-\varphi_0)}\sum_{n=0}^{\infty}\varepsilon_n\cos[\nu_n(\varphi-\varphi')] \times J_{\nu_n}(k_0\rho)H_{\nu_n}^{(2)}(k_0\rho'), \qquad (28)$$

where $\nu_n=n\pi/(\pi-\varphi_0)$ and

$$\varepsilon_n = \begin{cases} 1 & \text{if } n\geq1 \\ \frac{1}{2} & \text{if } n=0 \end{cases}. \qquad (29)$$

Regarding the $\rho>\rho'$ case, if we employ the $2J_\nu(z)=H_\nu^{(1)}(z)+H_\nu^{(2)}(z)$ identity and note that the

$$e^{\varepsilon\nu^2}H_\nu^{(1)}(k_0\rho)H_\nu^{(2)}(k_0\rho')\frac{\cos[\nu(\varphi_0-\pi+|\varphi-\varphi'|)]}{\sin[\nu(\pi-\varphi_0)]}$$

formula as well as its counterpart with ρ,ρ' interchanged, are odd functions of ν, Eq. (24) is derived (however, with ρ,ρ' interchanged). Hence, after the aforementioned path deformation and the application of the residues theorem,

$$E_{1z}(\rho,\varphi)=\frac{j\pi}{2(\pi-\varphi_0)}\sum_{n=0}^{\infty}\varepsilon_n\cos[\nu_n(\varphi-\varphi')]\times J_{\nu_n}(k_0\rho')H_{\nu_n}^{(2)}(k_0\rho). \qquad (30)$$

In an exactly analogous manner, it can be shown that

$$E_{2z}(\rho,\varphi)=\frac{j\pi}{2(\pi-\varphi_0)}\sum_{n=0}^{\infty}\varepsilon_n\cos[\nu_n(2\pi-\varphi-\varphi')]\times J_{\nu_n}(k_0\rho_<)H_{\nu_n}^{(2)}(k_0\rho_>), \qquad (31)$$

with $\rho_<\equiv\min(\rho,\rho')$ and $\rho_>\equiv\max(\rho,\rho')$. The procedure is completed via the verification that the second-kind KL transform of $E_{1z}(\rho,\varphi)$ and $E_{2z}(\rho,\varphi)$, as provided in Eqs. (28), (30), and (31), coincide with Eqs. (22) and (23). Remember that such a validation is enforced by the nonreciprocal nature of Eqs. (2) and (3). Indeed, through the mathematical analysis presented in the Appendix, it is proven that Eqs. (28), (30), and (22), as well as Eqs. (31) and (23) constitute pairs of KL-IKL transforms. Furthermore, notice that Eqs. (28), (30), and (31) coincide with Eq. (16) of Ref. 24, after an anticlockwise $\varphi_0/2$ coordinates rotation.

Figure 5 displays two quiver plots of the Poynting vector, as computed from Eqs. (28), (30), and (31) for $\varphi_0=30°$, $\varphi'=20°$, $40°$, and $\rho'=4\lambda_0$, where $\lambda_0=2\pi/k_0$ is the wavelength in the air. It is apparent that for $\varphi'=40°>\varphi_0$, the energy flow is in very good agreement with that predicted via the optical-ray approximation method. Conversely, when $\varphi'=20°<\varphi_0$ (i.e., violation of the principal assumptions set for the solution), a nonphysical source at $\varphi=320°$ and an "energy sink" at $\varphi=340°$ appear. This phenomenon can be exclusively attributed to the fact that the latter outcome has been obtained by utilizing a radiation condition which is not at all valid for the specific φ' value. The last explanation certifies our previous allegation that the choice of this condition plays a decisive role in the consistent application of the KL transform.

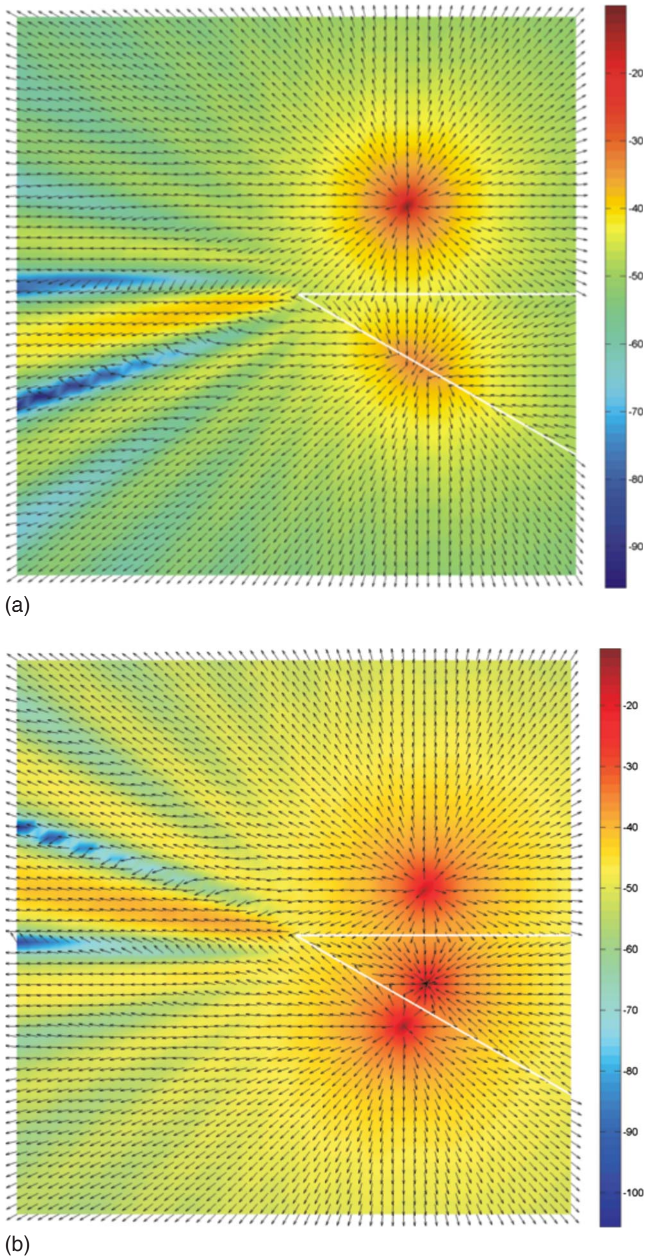

FIG. 5. (Color online) Power-flow diagrams obtained via Eqs. (28), (30), and (31) for $\varphi_0=30°$, $\rho'=4\lambda_0$ and (a) $\varphi'=40°$, (b) $\varphi'=20°$. The white solid line indicates the sides of the DNG wedge.

IV. $\varphi'<\varphi_0$ CASE

A. Analytical formulation

The objective of this section is to examine the $\varphi'<\varphi_0$ case of the metamaterial wedge-scattering problem. Let us recur to Fig. 3 and the optical-ray approach, by means of which we can deduce that the energy flows inward in region $\varphi_3<\varphi<\varphi_1$ (air) and outward in region $\varphi_1<\varphi<\varphi_2$ (DNG medium). Moreover, recalling that in a DNG material the energy flow and the phase advance have opposite directions, it is inferred that the electric field intensity varies proportionally to an $e^{jk_0\rho}/\sqrt{\rho}$ term, for large ρ, in both of the prior angular sectors, hence indicating

$$\lim_{\rho\to\infty}\sqrt{\rho}\left(\frac{\partial E_z}{\partial\rho}-jk_0E_z\right)=0 \qquad (32)$$

as the most suitable radiation condition for $\varphi_3<\varphi<\varphi_2$. On the other hand, Eq. (14) remains, still, valid for $0<\varphi<\varphi_3$ and $\varphi_2<\varphi<2\pi$. Therefore, based on these remarks, our space must be separated into four distinct areas: $0<\varphi<\varphi_3$ (region 1), $\varphi_3<\varphi<\varphi_1$ (region 2), $\varphi_1<\varphi<\varphi_2$ (region 3), and $\varphi_2<\varphi<2\pi$ (region 4). Following the procedure of Sec. II, a KL transform of the first kind is applied in regions 2 and3 and a KL transform of the second kind is applied in regions 1 and 4. So, if E_{iz} is the electric field intensity in the

ith region ($i=1,2,3,4$), the transformed fields are described by

$$\tilde{E}_{1z}(\nu;\varphi) = \mathrm{KL}_2\{E_{1z}(\rho,\varphi)\} = a_1(\nu)\cos(\nu\varphi) + b_1(\nu)\sin(\nu\varphi) + \frac{H_\nu^{(2)}(k_0\rho')}{2\nu\sin(\nu\pi)}\cos[\nu(\pi-|\varphi-\varphi'|)], \tag{33}$$

$$\tilde{E}_{2z}(\nu;\varphi) = \mathrm{KL}_1\{E_{2z}(\rho,\varphi)\} = a_2(\nu)\cos(\nu\varphi) + b_2(\nu)\sin(\nu\varphi), \tag{34}$$

$$\tilde{E}_{3z}(\nu;\varphi) = \mathrm{KL}_1\{E_{3z}(\rho,\varphi)\} = a_3(\nu)\cos(\nu\varphi) + b_3(\nu)\sin(\nu\varphi), \tag{35}$$

$$\tilde{E}_{4z}(\nu;\varphi) = \mathrm{KL}_2\{E_{4z}(\rho,\varphi)\} = a_4(\nu)\cos(\nu\varphi) + b_4(\nu)\sin(\nu\varphi). \tag{36}$$

Unknown functions $a_i(\nu), b_i(\nu)$ ($i=1,2,3,4$) are specified by the boundary conditions at region interfaces, i.e.,

$$E_{1z}|_{\varphi=\varphi_3} = E_{2z}|_{\varphi=\varphi_3}, \qquad \left.\frac{\partial E_{1z}}{\partial\varphi}\right|_{\varphi=\varphi_3} = \left.\frac{\partial E_{2z}}{\partial\varphi}\right|_{\varphi=\varphi_3}, \tag{37a}$$

$$E_{2z}|_{\varphi=\varphi_1} = E_{3z}|_{\varphi=\varphi_1}, \qquad \left.\frac{\partial E_{2z}}{\partial\varphi}\right|_{\varphi=\varphi_1} = -\left.\frac{\partial E_{3z}}{\partial\varphi}\right|_{\varphi=\varphi_1}, \tag{37b}$$

$$E_{3z}|_{\varphi=\varphi_2} = E_{4z}|_{\varphi=\varphi_2}, \qquad \left.\frac{\partial E_{3z}}{\partial\varphi}\right|_{\varphi=\varphi_2} = \left.\frac{\partial E_{4z}}{\partial\varphi}\right|_{\varphi=\varphi_2}, \tag{37c}$$

$$E_{4z}|_{\varphi=2\pi} = E_{1z}|_{\varphi=0}, \qquad \left.\frac{\partial E_{4z}}{\partial\varphi}\right|_{\varphi=2\pi} = -\left.\frac{\partial E_{1z}}{\partial\varphi}\right|_{\varphi=0}. \tag{37d}$$

As a subsequent step, we define the operator $\mathcal{L}[\tilde{f}(\nu)] = \mathrm{KL}_1\{\mathrm{IKL}_2[\tilde{f}(\nu)]\}$, which, given the second-kind KL transform $\tilde{f}(\nu)$ of an arbitrary function $f(x)$, provides the first-kind KL transform of $f(x)$. It is mentioned that due to the nonreciprocal property of KL and IKL transforms, $\mathcal{L}$ is, only, appropriate for functions that are known to be the second-kind KL transforms of other functions. Thus, applying the first-kind KL transform to Eqs. (37a)–(37c) via operator $\mathcal{L}$, where necessary, and the second-kind KL transform to Eq. (37d), it is derived,

$$\mathcal{L}\{\tilde{E}_{1z}\}|_{\varphi=\varphi_3} = \tilde{E}_{2z}|_{\varphi=\varphi_3}, \qquad \mathcal{L}\left.\left\{\frac{\partial\tilde{E}_{1z}}{\partial\varphi}\right\}\right|_{\varphi=\varphi_3} = \left.\frac{\partial\tilde{E}_{2z}}{\partial\varphi}\right|_{\varphi=\varphi_3}, \tag{38a}$$

$$\tilde{E}_{2z}|_{\varphi=\varphi_1} = \tilde{E}_{3z}|_{\varphi=\varphi_1}, \qquad \left.\frac{\partial\tilde{E}_{2z}}{\partial\varphi}\right|_{\varphi=\varphi_1} = -\left.\frac{\partial\tilde{E}_{3z}}{\partial\varphi}\right|_{\varphi=\varphi_1}, \tag{38b}$$

$$\tilde{E}_{3z}|_{\varphi=\varphi_2} = \mathcal{L}\{\tilde{E}_{4z}\}|_{\varphi=\varphi_2}, \qquad \left.\frac{\partial\tilde{E}_{3z}}{\partial\varphi}\right|_{\varphi=\varphi_2} = \mathcal{L}\left.\left\{\frac{\partial\tilde{E}_{4z}}{\partial\varphi}\right\}\right|_{\varphi=\varphi_2}, \tag{38c}$$

$$\tilde{E}_{4z}|_{\varphi=2\pi} = \tilde{E}_{1z}|_{\varphi=0}, \qquad \left.\frac{\partial\tilde{E}_{4z}}{\partial\varphi}\right|_{\varphi=2\pi} = -\left.\frac{\partial\tilde{E}_{1z}}{\partial\varphi}\right|_{\varphi=0}. \tag{38d}$$

Furthermore, if Eqs. (33)–(36) are plugged into Eq. (38),

$$\mathcal{L}\left\{\mathbf{M}_\nu(\varphi_3)\cdot\mathbf{X}_1(\nu) + \frac{H_\nu^{(2)}(k_0\rho')}{2\nu\sin(\nu\pi)}\mathbf{S}_\nu(2\varphi_0-\pi)\right\} = \mathbf{M}_\nu(\varphi_3)\cdot\mathbf{X}_2(\nu), \tag{39a}$$

$$\mathbf{M}_\nu(\varphi_1)\cdot\mathbf{X}_2(\nu) = \mathbf{J}\cdot\mathbf{M}_\nu(\varphi_1)\cdot\mathbf{X}_3(\nu), \tag{39b}$$

$$\mathbf{M}_\nu(\varphi_2)\cdot\mathbf{X}_3(\nu) = \mathcal{L}\{\mathbf{M}_\nu(\varphi_2)\cdot\mathbf{X}_4(\nu)\}, \tag{39c}$$

$$\mathbf{M}_\nu(2\pi)\cdot\mathbf{X}_4(\nu) = \mathbf{J}\cdot\mathbf{M}_\nu(0)\cdot\mathbf{X}_1(\nu) + \frac{H_\nu^{(2)}(k_0\rho')}{2\nu\sin(\nu\pi)}\mathbf{S}_\nu(\pi-\varphi'), \tag{39d}$$

where $\mathbf{X}_i(\nu)=[a_i(\nu)b_i(\nu)]^T$ ($i=1,2,3,4$), $\mathbf{S}_\nu(a) = [\cos(\nu a)\nu\sin(\nu a)]^T$, T denotes the transpose of a matrix,

$$\mathbf{M}_\nu(a) = \begin{bmatrix} \cos(\nu a) & \sin(\nu a) \\ -\nu\sin(\nu a) & \nu\cos(\nu a) \end{bmatrix} \tag{40}$$

and $\mathbf{J}$ is a 2×2 diagonal matrix with diagonal elements 1 and -1. Solving the system of linear Eq. (39) with respect to $a_1(\nu), b_1(\nu)$, it is extracted,

$$\mathcal{L}\Bigg(a_1(\nu)[\cos(\nu\varphi_3)-\cos(\nu\varphi')] + b_1(\nu)[\sin(\nu\varphi_3)-\sin(\nu\varphi')] + \frac{H_\nu^{(2)}(k_0\rho')}{2\nu\sin(\nu\pi)}\{\cos[\nu(2\varphi_0-\pi)]-\cos(\nu\pi)\}\Bigg) = 0, \tag{41a}$$

$$\mathcal{L}\Bigg(\nu a_1(\nu)[\sin(\nu\varphi_3)-\sin(\nu\varphi')] - \nu b_1(\nu)[\cos(\nu\varphi_3) - \cos(\nu\varphi')] - \frac{H_\nu^{(2)}(k_0\rho')}{2\sin(\nu\pi)}\{\sin[\nu(2\varphi_0-\pi)]+\sin(\nu\pi)\}\Bigg) = 0. \tag{41b}$$

The crux for having the latter formulas solved resides on the fact that the sole solution of equation $\mathcal{L}\{\tilde{f}(\nu)\}=0$ is the zero function $\tilde{f}(\nu)=0$. This remark constitutes an immediate upshot of the statement that the only function whose KL transform equals to zero, is the zero function. Therefore, the operand in Eq. (41) is zero and $a_1(\nu), b_1(\nu)$ are attained to be the same as in Eqs. (20a) and (20b). In turn, $a_4(\nu), b_4(\nu)$, calculated through Eq. (39d), coincide with $a_2(\nu), b_2(\nu)$ of Eqs. (21a) and (21b). Generally, $E_{1z}(\rho,\varphi)$ is the same as in Eqs. (28) and (30) and $E_{4z}(\rho,\varphi)$ coincides with $E_{2z}(\rho,\varphi)$ in Eq. (31).

For $a_2(\nu), b_2(\nu)$, substitution of Eq. (20) into Eq. (39a) yields

$$\mathbf{X}_2(\nu) = \mathbf{M}_\nu^{-1}(\varphi_3) \cdot \mathcal{L}\left\{ \frac{H_\nu^{(2)}(k_0\rho')}{2\nu \sin[\nu(\pi - \varphi_0)]} \mathbf{S}_\nu(\varphi_0 - \pi) \right\}, \tag{42}$$

while, through Eq. (39b), $a_3(\nu), b_3(\nu)$ are found from

$$\mathbf{X}_3(\nu) = \mathbf{M}_\nu^{-1}(\varphi_1) \cdot \mathbf{J} \cdot \mathbf{M}_\nu(\varphi_1) \cdot \mathbf{X}_2(\nu). \tag{43}$$

Thereupon, quantities

$$A = \mathcal{L}\left\{ \frac{H_\nu^{(2)}(k_0\rho')}{2\nu} \cot[\nu(\pi - \varphi_0)] \right\}, \tag{44}$$

$$B = \mathcal{L}\left\{ -\frac{1}{2} H_\nu^{(2)}(k_0\rho') \right\}, \tag{45}$$

must be evaluated. Through the definition of operator $\mathcal{L}$, in order to obtain $\mathcal{L}\{\tilde{f}(\nu)\}$, function $f(x)$ should be, first, computed by Eq. (3) with $i=2$. Then, it is necessary to verify if the second-kind KL transform of $f(x)$ is, actually, $\tilde{f}(\nu)$, and, lastly, get the first-kind KL transform of $f(x)$. Application of the preceding process to A leads to the calculation of the operand's second-type IKL transform, in terms of the contour deformation technique presented in Sec. II, as

$$\mathrm{IKL}_2\left\{ \frac{H_\nu^{(2)}(k_0\rho')}{2\nu} \cot[\nu(\pi - \varphi_0)] \right\} = \frac{j\pi}{2(\pi - \varphi_0)} \sum_{n=0}^{\infty} \varepsilon_n J_{\nu_n}(k_0\rho_<) H_{\nu_n}^{(2)}(k_0\rho_>). \tag{46}$$

Using the results of the Appendix, it can be proven that the second-type KL transform on the right-hand side of Eq. (46) is, indeed, the operand on the right-hand side of Eq. (44). So, A is retrieved from (see Appendix for the full analysis)

$$A = \mathrm{KL}_1\left\{ \frac{j\pi}{2(\pi - \varphi_0)} \sum_{n=0}^{\infty} \varepsilon_n J_{\nu_n}(k_0\rho_<) H_{\nu_n}^{(2)}(k_0\rho_>) \right\} = \frac{H_\nu^{(1)}(k_0\rho')}{2\nu} \cot[\nu(\pi - \varphi_0)] - \frac{2}{\pi - \varphi_0} \sum_{n=0}^{\infty} \varepsilon_n e^{j\nu_n\pi/2} J_{\nu_n}(k_0\rho') \frac{e^{-j\nu\pi/2}}{\nu^2 - \nu_n^2}. \tag{47}$$

In contrast, to find B is simpler, since one may notice that $H_\nu^{(2)}(k_0\rho')$ is the second-type KL transform of $\rho\delta(\rho-\rho')$, i.e.,

$$B = \mathrm{KL}_1\left\{ -\frac{1}{2}\rho\delta(\rho - \rho') \right\} = -\frac{1}{2} H_\nu^{(1)}(k_0\rho'). \tag{48}$$

Therefore, by means of Eqs. (42) and (43), it is derived

$$a_2(\nu) = A\cos(\nu\varphi_3) - B\sin(\nu\varphi_3), \tag{49a}$$

$$b_2(\nu) = A\sin(\nu\varphi_3) + B\cos(\nu\varphi_3), \tag{49b}$$

$$a_3(\nu) = A\cos(\nu\varphi_2) + B\sin(\nu\varphi_2), \tag{50a}$$

$$b_3(\nu) = A\sin(\nu\varphi_2) - B\cos(\nu\varphi_2). \tag{50b}$$

Finally, Eq. (34) becomes

$$\tilde{E}_{2z}(\nu;\varphi) = \frac{H_\nu^{(1)}(k_0\rho')}{2\nu} \frac{\cos[\nu(\pi - \varphi_0 + \varphi' - \varphi)]}{\sin[\nu(\pi - \varphi_0)]} - \frac{2}{\pi - \varphi_0} \sum_{n=0}^{\infty} \varepsilon_n e^{j\nu_n\pi/2} J_{\nu_n}(k_0\rho') \frac{e^{-j\nu\pi/2}}{\nu^2 - \nu_n^2} \times \cos[\nu(\varphi - \varphi_3)] \tag{51}$$

whereas from Eq. (35) one receives

$$\tilde{E}_{3z}(\nu;\varphi) = \frac{H_\nu^{(1)}(k_0\rho')}{2\nu} \frac{\cos[\nu(\pi + \varphi_1 - \varphi' - \varphi)]}{\sin[\nu(\pi - \varphi_0)]} - \frac{2}{\pi - \varphi_0} \sum_{n=0}^{\infty} \varepsilon_n e^{j\nu_n\pi/2} J_{\nu_n}(k_0\rho') \frac{e^{-j\nu\pi/2}}{\nu^2 - \nu_n^2} \times \cos[\nu(\varphi - \varphi_2)]. \tag{52}$$

Having extracted the electric field intensity KL transform, the spatial distribution of the field may be readily acquired from Eq. (3). Hence, after the proper mathematical manipulations, the IKL-transform integral of $\tilde{E}_{2z}(\nu;\varphi)$ is written as

$$\mathrm{IKL}_1\{\tilde{E}_{2z}(\nu;\varphi)\} = \frac{j\pi}{2(\pi - \varphi_0)} \sum_{n=0}^{\infty} \varepsilon_n \cos[\nu(\varphi - \varphi')] J_{\nu_n}(k_0\rho_<) H_{\nu_n}^{(2)}(k_0\rho_>). \tag{53}$$

Bear in mind that the IKL_1 notation is, unduly, used to point out the integral of Eq. (3) since it is not known, yet, whether the KL transform of the right-hand side of Eq. (53) equals to $\tilde{E}_{2z}(\nu;\varphi)$. In addition, the IKL integral of the first term on the right-hand side of Eq. (51) has been computed in a formalistic way, as it does not converge for every ρ, due to the fact that $|\pi-\varphi_0+\varphi'-\varphi|-|\pi-\varphi_0|>0$, for $\varphi>\varphi_3$. At a first glance, the outcome of Eq. (53) seems inadequate since it is the same as Eqs. (28) and (30) which result in artificial sources and "energy sinks." Nonetheless, a closer assessment reveals that the first-kind KL transform of Eq. (53), described by

$$\mathrm{KL}_1\{\mathrm{IKL}_1[\tilde{E}_{2z}(\nu;\varphi)]\} = \frac{H_\nu^{(1)}(k_0\rho')}{2\nu} \frac{\cos[\nu(\pi - \varphi_0 + \varphi' - \varphi)]}{\sin[\nu(\pi - \varphi_0)]} - \frac{2}{\pi - \varphi_0} \sum_{n=0}^{\infty} \varepsilon_n e^{j\nu_n\pi/2} J_{\nu_n}(k_0\rho') \frac{e^{-j\nu\pi/2}}{\nu^2 - \nu_n^2} \times \cos[\nu_n(\varphi - \varphi')], \tag{54}$$

(see Appendix for details), differs from $\tilde{E}_{2z}(\nu;\varphi)$ given in Eq. (51). This observation enables us to realize that, essentially, there is no function $E_{2z}(\rho,\varphi)$ whose first-kind KL transform is the same as the one of Eq. (51). Similar conclusions are, also, drawn for $\tilde{E}_{3z}(\nu;\varphi)$ in Eq. (52).

B. Discussion

In general, the field of a DNG wedge with $\epsilon_r=\mu_r=-1$, illuminated by a current source, diverges inside the angular sector $\varphi_3 < \varphi < \varphi_2$, when $\varphi' < \varphi_0$. Nevertheless, this behavior is not surprising, if we consider that such a phenomenon is, also, present in a planar metamaterial slab, where the field cannot be evaluated between the first focus in the interior and the second focus at the exterior of the slab. Due to its significance, a comprehensive explanation of the prior issues is next provided. Actually, the most intriguing effect related to the ideal DNG wedge is that the electric field intensity on the $\varphi = \varphi_2$ and $\varphi = \varphi_3$ planes is exactly the same as in the source plane, implying that the line source is perfectly focused on the aforesaid planes. For this situation to occur, both the propagating and evanescent part of the source's spectrum have to be perfectly reproduced at the focus. Regarding propagating waves, it is the negative refraction that leads to the perfect focusing of their energy, as indicated in the ray diagram of Fig. 3. One can clearly observe that all rays captured from the wedge converge at two specific points inside and outside the DNG material. In other words, all of the propagating spectrum energy captured by the DNG medium is perfectly focused at these two particular points.

Conversely, transmission of evanescent waves lies on a completely different principle. Specifically, since the amplitude of these waves decays with the distance from the source in free space, the imaging device should posses an amplification mechanism in order to restore their amplitude at the focus. In the planar-slab geometry, the excitation of surface-plasmon modes at the air-DNG interfaces results in the concentration of the energy, required for the reproduction of the evanescent waves amplitude at the focus, around these interfaces.[5,15] Similarly, the DNG wedge supports plasmon modes, whose amplitude maximizes on the air-DNG interfaces and decays exponentially along the φ direction away from them.[19,21] The attenuation factor ν_p of these modes toward the φ direction obeys to dispersion equations

$$\mu_r = -\frac{\tanh[\nu_p(\pi - \varphi_0/2)]}{\tanh(\nu_p \varphi_0/2)}, \tag{55a}$$

$$\mu_r = -\frac{\tanh(\nu_p \varphi_0/2)}{\tanh[\nu_p(\pi - \varphi_0/2)]}, \tag{55b}$$

holding for even and odd modes, with regard to the bisector $\varphi = -\varphi_0/2$ of the wedge.[19] From Eq. (55) it can be, easily, derived that, when $\mu_r = -1$, $|\nu_p| \to \infty$, which explains the perfect focusing of the entire evanescent part of the spectrum (i.e., infinite resolution). Recall from the planar-slab case that the value of the plasmon's spectral variable determines the portion of evanescent waves that can be transmitted to the focus.

A phenomenon which is closely associated to the excitation of plasmon modes is field divergence in the sector between the focuses. Its interpretation lies on the fact that, when $|\nu_p| \to \infty$, even and odd modes acquire infinite amplitude in this sector as well as in its symmetric one with respect to $\varphi = -\varphi_0/2$. Essentially, in the latter sector the modes add destructively while in the former constructively, yielding a diverging field only between the two focuses. As a matter of fact, apart from this diverging behavior, the field possesses an additional singularity near the tip of the wedge, which becomes observable when μ_r is slightly different from 1 and, therefore from Eq. (55), ν_p is finite. In particular, for small ρ values, the φ component of the magnetic field intensity behaves as $\rho^{\pm j\nu_p - 1}$,[19] yielding a ρ^{-2} dependence of the magnetic energy density. Alternatively, magnetic energy density is hypersingular near the wedge tip and the total magnetic energy becomes infinite. Furthermore, it is noteworthy to point out the infinitely rapid oscillating behavior of all field components as $\rho \to 0$, following from the $\rho^{\pm j\nu_p} = e^{\pm j\nu_p \ln \rho}$ term in their expressions. Evidently, the previously described nonphysical phenomena are suppressed in a more realistic configuration, where losses are present,[30] however, with the simultaneous degradation in imaging resolution.

As already indicated in Sec. II, dissipation is an indispensable part of DNG materials,[30] although it may be considered small in the $\epsilon_r = \mu_r = -1$ case. Regarding the perfect imaging effect, losses affect propagating and evanescent waves in a different regime. Thus, for propagating waves, dissipation introduces a reduction in their amplitude, but it has a little effect on their focusing, since it does not notably influence negative refraction. Conversely, evanescent waves are significantly affected, even, by small losses, and the infinite resolution of a lossless DNG wedge is restricted to finite values, although still above the diffraction limit. Specifically, if μ_r has an imaginary part, ν_p becomes finite and complex, imposing an upper limit on the evanescent waves spectrum which can be transmitted to the focus.[33] Assuming that $\nu_p = \nu_p' + j\nu_p''$, the E_z dependence near the wedge tip is proportional to $\rho^{j\nu_p} = \rho^{j\nu_p'} \rho^{-\nu_p''}$, with $\nu_p'' < 0$ since the tangential field components to the edge must be finite. Consequently, H_φ behaves like $\rho^{j\nu_p'} \rho^{-\nu_p'' - 1}$ and the energy singularity disappears, as $-\nu_p'' - 1 > -1$. In addition, the finite value of ν_p' suppresses field divergence between the focuses, despite the fact that amplitude may receive large values.

V. NUMERICAL RESULTS

To verify the preceding analysis, this section conducts a set of comparisons between the proposed field expressions and diverse numerical outcomes, obtained via a frequency-dependent FDTD technique. Due to the inevitably confined size of the computational domain and thus its lack to simulate infinite structures, our geometry is truncated at a radius R from the origin by means of a complex-frequency-shifted perfectly matched layer.[27] Moreover, the finite wedge is terminated at a circular arc for the elimination of any artificial reflections (see the white solid-line sketch in Fig. 6) while a $\lambda_0/20$ spatial step, with λ_0 the free-space wavelength at $f_0 = 1$ GHz, is selected to discretize the continuous space. The constitutive parameters of the DNG material are described by a Drude dispersion model, which gives $\epsilon_r = \mu_r = -1$ at 1 GHz, and the distance between the source and the wedge apex is set to $\rho' = 4\lambda_0$.

Considering the prior issues, the first application deals with the numerical evaluation of the power flow when $\varphi_0 = 30°$ and $R = 20\lambda_0$. To this goal, Figs. 6(a) and 6(b) present the corresponding diagrams for $\varphi' = 40°$ and $\varphi' = 20°$, respectively. For the $\varphi' = 40°$ case and consistent with our ray-approximation analysis in Fig. 2, the power converges as it

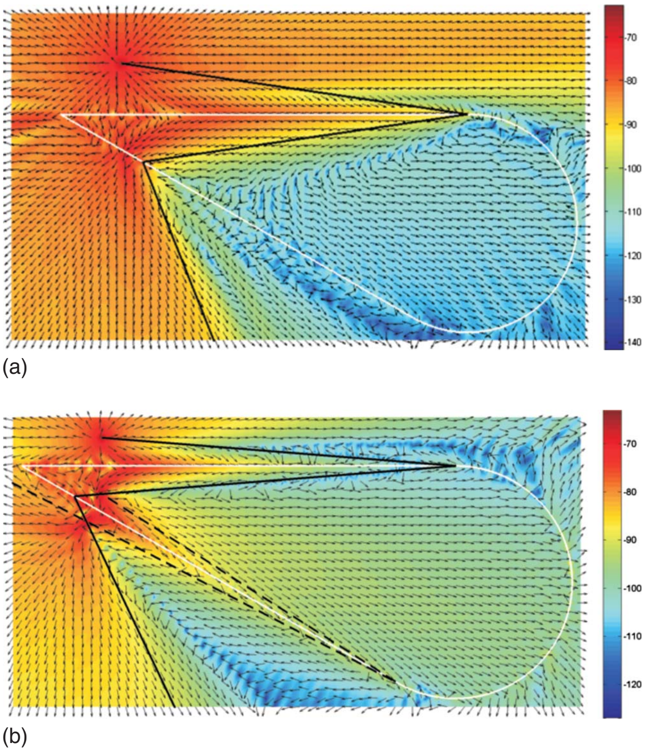

FIG. 6. (Color online) Numerically computed power-flow diagrams for $\varphi_0=30°$, $\rho'=4\lambda_0$ and (a) $\varphi'=40°$, (b) $\varphi'=20°$.

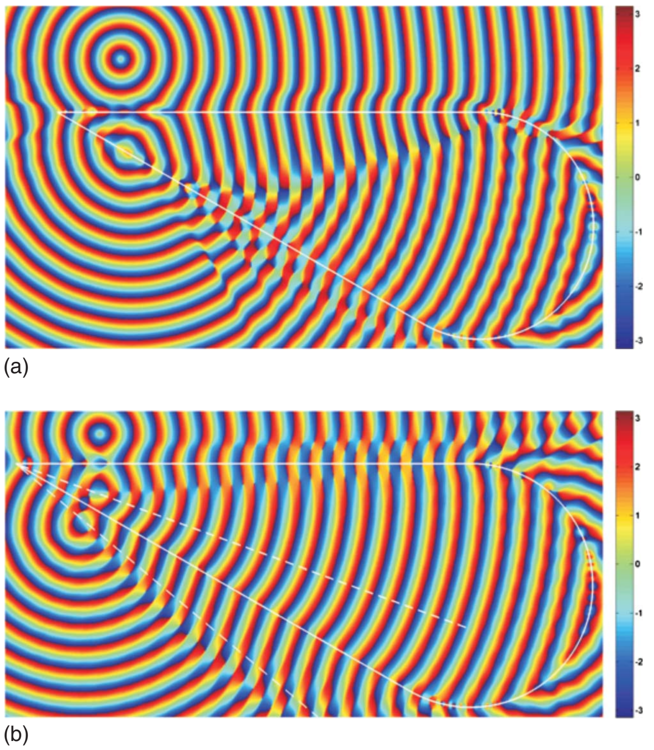

FIG. 7. (Color online) Numerically computed phase diagrams for $\varphi_0=30°$, $\rho'=4\lambda_0$ and (a) $\varphi'=40°$, (b) $\varphi'=20°$.

crosses the $\varphi=0°$ air-DNG interface (with all coordinates referring, hereafter, to Fig. 1) and diverges after passing through the $\varphi=\varphi_1$ one. Nevertheless, contrary to the theoretical presumptions, the area where incoming waves exist does not completely occupy the wedge sector. In fact, based on the power intensity amplitude of Fig. 6(a), it is observed that the ρ component of the Poynting vector points toward the wedge apex, primarily, in the region defined by the wedge sides and the black solid line. Note that the latter line is symmetrical—with regard to the upper wedge side—to the last ray on the right-hand side of the source which intersects the metamaterial. This simply indicates that any discrepancies between numerical and theoretical results should be, above all, attributed to the finite length of the structure. Also, the refracted power is, principally, located on the left-hand side of the black solid line below the wedge. Equivalent conclusions are drawn for the $\varphi'=20°$ case, with the exception that, herein, two focal points are created, namely, one inside and the other outside the wedge, as already explained in Fig. 3. Again, the last ray of the source that reaches the structure [black solid line in Fig. 6(b)] specifies the region between the source and the first focus where incoming waves exist. Also, for $\varphi<\varphi_3$, the power intensity becomes significant in the area between the black solid and the dashed line, which connects the second focus to the end point of the wedge's $\varphi=\varphi_1$ side. In particular, this line is formed by the last ray, emanating from the first focus in the metamaterial, that is, refracted by the $\varphi=\varphi_1$ air-DNG interface.

Similar interpretations are extracted from the phase of the field, illustrated in Figs. 7(a) and 7(b). Recollecting that the phase grows/reduces with the distance from the origin for incoming/outgoing waves in the air and outgoing/incoming waves in the DNG medium, one can, readily, discern the regions where each wave type evolves and confirm that are the same as those depicted by the ray-approximation method (except for the effects accredited to the metamaterial's finite size). It is mentioned that the white dotted lines inside and outside the DNG medium in Fig. 7(b) correspond, respectively, to the $\varphi=\varphi_2$ and $\varphi=\varphi_3$ lines of Fig. 3.

Next, our investigation validates the efficiency of the analytically derived near-field expressions through comparisons with numerical data for different φ_0 and φ' values. All verifications are performed along straight lines, whose end points A and B have coordinates (x_A, y_A) and (x_B, y_B), with respect to the system of Fig. 1. In this context, the real part of the electric field intensity for the $\varphi_0=30°, \varphi'=40°$ case is presented in Fig. 8(a) along the line with $x_A=-0.705$ m, $y_A=0.45$ m, $x_B=1.469$ m, $y_B=-3.3150$ m and in Fig. 8(b) along the line with $x_A=-0.705$ m, $x_B=7.74$ m, $y_A=y_B=0.45$ m. For the sake of convenience, these lines are drawn in the respective inlet figures, which show the surface plot of the electric field intensity real part. Additionally, based on the aspects of the preceding power-flow analysis, they are, carefully, chosen to lie in areas where the effect of the wedge's finite length is deemed small. On the other hand, the horizontal axis of Figs. 8(a) and 8(b) provides the distance from point A in wavelengths whereas their vertical axis gives the electric field intensity in arbitrary units (arb. units). As promptly observed, the plots in both figures exhibit a very satisfactory agreement, thus substantiating the potential of the analytical formulas.

In relation to the $\varphi'<\varphi_0$ case, it is important to take into consideration that the analytical solution does not converge

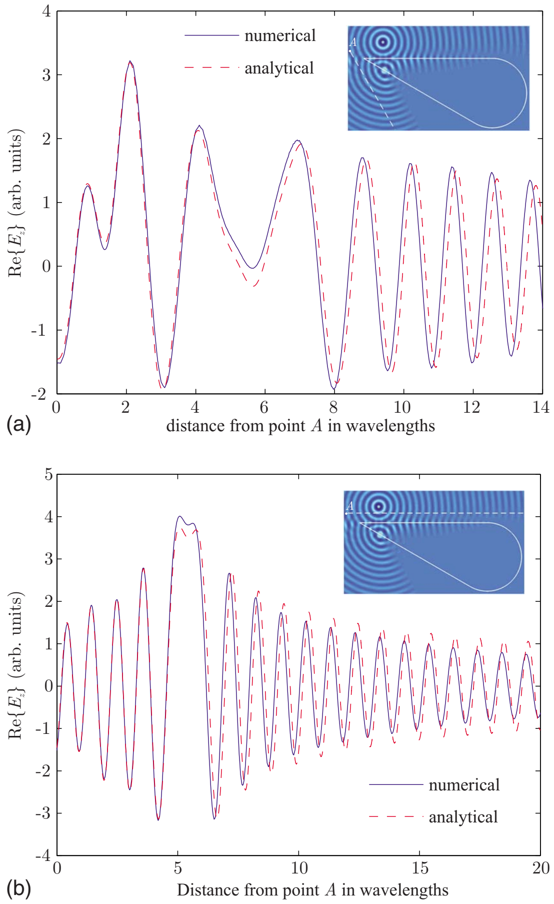

FIG. 8. (Color online) Comparison between the numerically and analytically calculated electric field intensity real part for $\varphi_0=30°$, $\rho'=4\lambda_0$, and $\varphi'=40°$ along the line with end-point coordinates (a) $x_A=-0.705$ m, $y_A=0.45$ m, $x_B=1.469$ m, $y_B=-3.315$ m and (b) $x_A=-0.705$ m, $x_B=7.74$ m, $y_A=y_B=0.45$ m.

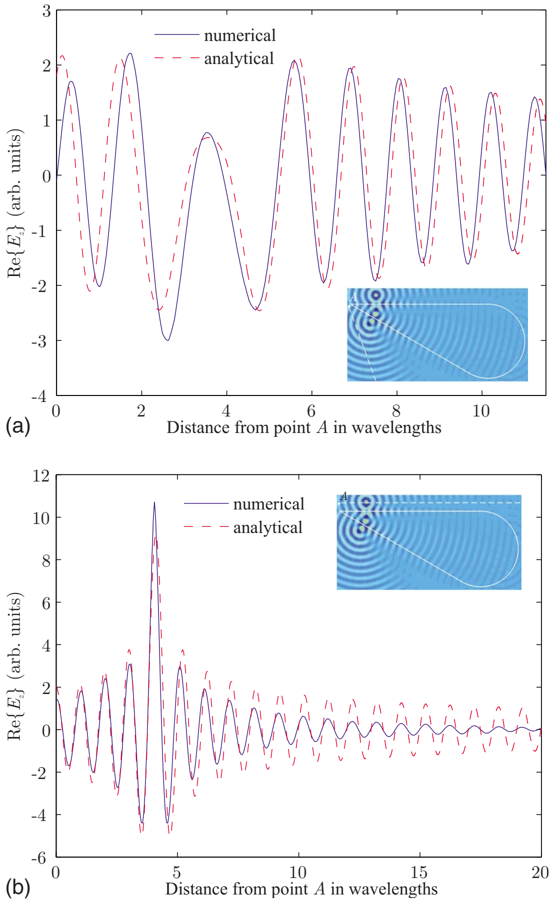

FIG. 9. (Color online) Comparison between the numerically and analytically calculated electric field intensity real part for $\varphi_0=30°$, $\rho'=4\lambda_0$, $\varphi'=20°$ along the line with end-point coordinates (a) $x_A=-0.105$ m, $y_A=0$ m, $x_B=1.102$ m, $y_B=-3.315$ m and (b) $x_A=-0.105$ m, $x_B=7.74$ m, $y_A=y_B=0.36$ m.

in the $\varphi_3<\varphi<\varphi_2$ angular sector and therefore no comparisons can be conducted therein. To this issue, remember that the region where the structure's finite size appears negligible is not only determined by the last ray of the source crossing the DNG medium but, also, from the ray that passes from the second focus and the wedge's end point at its $\varphi=\varphi_1$ side [dashed line in Fig. 6(b)]. On the base of these remarks, the analytically and numerically evaluated real part of the electric field intensity for $\varphi_0=30°$ and $\varphi'=20°$, is presented in Figs. 9(a) and 9(b) along the lines with $x_A=-0.105$ m, $y_A=0$ m, $x_B=1.102$ m, $y_B=-3.315$ m and $x_A=-0.105$ m, $x_B=7.74$ m, $y_A=y_B=0.36$ m, respectively. Their agreement is, evidently, very sufficient, implying that, although the analytical solution is nonconvergent for $\varphi_3<\varphi<\varphi_2$, it remains considerably accurate in the rest domain.

To strengthen the last assertion, the $\varphi_0=60°$ and $\varphi'=30°$ case is, additionally, explored. Bewaring to conduct our comparison in areas where the wedge's finite length has a minimal impact on the field, the outcomes along the lines with $x_A=0$ m, $x_B=-0.705$ m, $y_A=y_B=-1.2$ m and $x_A=-0.705$ m, $x_B=15.9$ m, $y_A=y_B=0.36$ m are displayed in Figs. 10(a) and 10(b). Again, it becomes apparent that the analytical and numerical curves are, appreciably, close to each other. On the contrary, if the perpendicular to the x-axis line passing from the $(x_A,y_A)=(-0.6$ m$,0$ m$)$ point is to be selected, the curves agree, merely, on the part of the line which belongs to the region where the structure's finite size can be neglected, as shown in shaded area of Fig. 11. The above observations confirm the robustness of the proposed infinite case closed-form expressions and manifest the key prerequisites for the consistent application of them in the finite arrangement.

VI. CONCLUSION

The analytical solution for the problem of a lossless DNG wedge illuminated by a line source at an arbitrary position, has been presented in this paper via an efficiently formulated technique founded on the KL transform. Establishing a self-consistent mathematical procedure, it has been proven that when the KL transform is applied to the Helmholtz equation, the method inherently embodies the radiation condition. Hence, to extract physically meaningful results, one must, first, determine the proper radiation condition, which, in this paper, has been attained by a ray-tracing algorithm. Furthermore, when the source lies in an angular sector equal to the

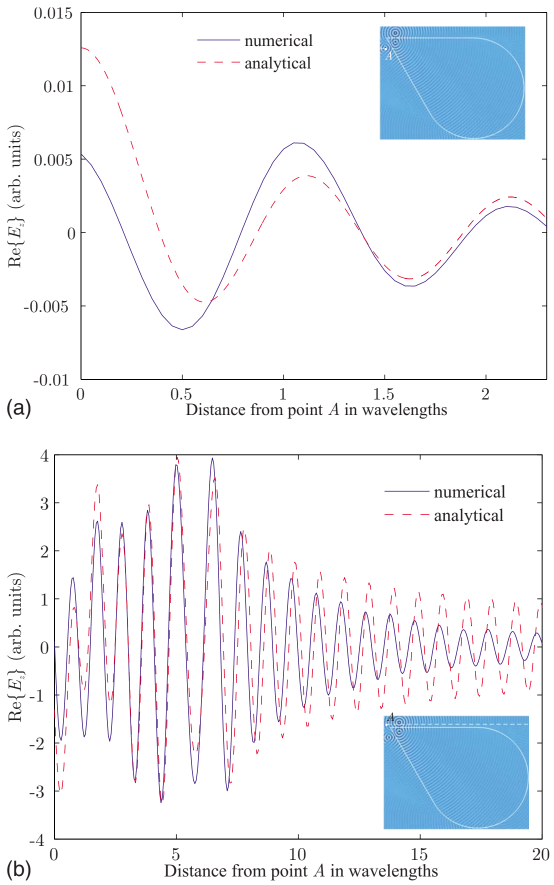

FIG. 10. (Color online) Comparison between the numerically and analytically calculated electric field intensity real part for $\varphi_0=60°$, $\rho'=4\lambda_0$, $\varphi'=30°$ along the line with end-point coordinates (a) $x_A=0$ m, $x_B=-0.705$ m, $y_A=y_B=-1.2$ m and (b) $x_A=-0.705$ m, $x_B=15.9$ m, $y_A=y_B=0.36$ m.

opening of the wedge, a linear operator that relates KL transforms of different kind has been introduced to transform both the Helmholtz equation and the boundary conditions in the KL domain. In this way, the transformed field is expressed as a direct combination of specific integrals, which, for the wedge examined herein, can be computed in a closed form. For the investigation to be complete, comparisons with FDTD outcomes have confirmed the high accuracy of the proposed formulas.

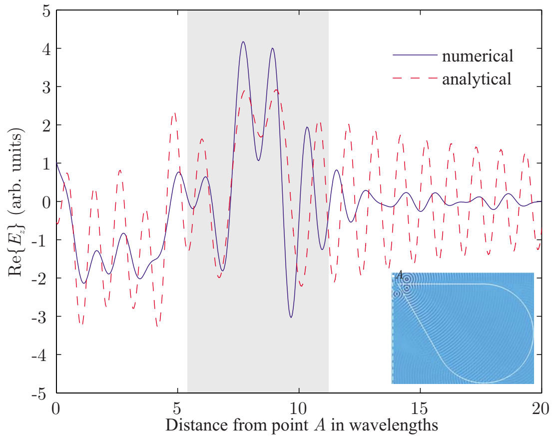

FIG. 11. (Color online) Comparison between the numerically and analytically calculated electric field intensity real part for $\varphi_0=60°$, $\rho'=4\lambda_0$, $\varphi'=30°$ along the perpendicular to the x-axis line passing from the (−0.6 m,0 m) point.

One of the analysis' major conclusions is that the ideal DNG wedge behaves similarly to the planar slab regarding its imaging characteristics. In particular, if the angular distance of the source is less than the wedge angle, the field on the source plane is, perfectly, reproduced on two planes, inside and outside the wedge. Moreover, as in the planar case, the field between the two focus planes diverges, due to the excitation of surface waves. The same results, still, hold in the finite case, with the exception that the field has to be examined in the area restricted by the last rays of the source which intersect the DNG medium. Finally, it is worth noticing that, unlike, the planar slab, the wedge is a semi-infinite structure and it does not capture all the source's rays, a phenomenon which, however, does not affect the imaging quality.

A possible future extension of the present work could be the investigation of the focusing characteristics of an infinite DNG wedge in the presence of a point source. Although focusing of a point source is, actually, a three-dimensional (3D) problem, it can be reduced to a corresponding two-dimensional (2D) one since the 3D field can be expressed via the 2D Green's function, which in fact is the electric field intensity obtained in the present paper. Moreover, from a qualitative point of view, an arbitrary ray impinging on one of the air-DNG interfaces is refracted at an angle opposite to the incident one, due to the -1 value of the refractive index. In other words, the refracted ray is symmetrical to its incident counterpart, with respect to the air-DNG interface. Therefore, provided that the incident ray emanates from the point source, the refracted one intersects the horizontal xy plane at a point symmetrical to the source, a fact which indicates that all rays captured by the wedge converge to this particular point inside the DNG medium. It is worth noticing that the point of convergence coincides with the focus inside the wedge of the 2D problem. Through a similar reasoning, it can be found that rays, also, intersect at an additional point outside the wedge, which is the other focus of the 2D configuration. The above remarks allow us to expect that a lossless DNG wedge maintains its imaging properties in the 3D space, as well.

ACKNOWLEDGMENTS

We would like to thank Vassilios Papantoniou of the Department of Electrical and Computer Engineering, Aristotle University of Thessaloniki, for his useful assistance. This work has been supported by the Greek General Secretariat of Research and Technology under Grant No. PENED03/03ED936.

APPENDIX: KL-TRANSFORM COMPUTATIONS IN EQS. (28) and (30)

It is the purpose of this section to provide a detailed description for the KL-transform evaluation of function

$$u(\rho) = \frac{j\pi}{2(\pi - \varphi_0)} \sum_{n=0}^{\infty} \varepsilon_n J_{\nu_n}(k_0\rho_<) H^{(2)}_{\nu_n}(k_0\rho_>) \cos[\nu_n(\varphi - \varphi')], \tag{A1}$$

that appears during the verification process of Eqs. (28) and (30) as well as in the determination of A from Eq. (44). Recall that $\nu_n = n\pi/(\pi - \varphi_0)$ while the value of ε_n is given in Eq. (29). Let us, first, obtain the KL transform of the $u_n(\rho) = J_{\nu_n}(k_0\rho_<)H^{(2)}_{\nu_n}(k_0\rho_>)$ function, which is the constitutive element of the sum in Eq. (A1). To this end, one may write

$$\begin{aligned} u_n(\rho) &= J_{\nu_n}(k_0\rho) H^{(2)}_{\nu_n}(k_0\rho')[H(\rho) - H(\rho - \rho')] \\ &\quad + J_{\nu_n}(k_0\rho') H^{(2)}_{\nu_n}(k_0\rho) H(\rho - \rho') \end{aligned} \tag{A2}$$

with $H(\rho)$ the Heaviside step function, and derive that $u_n(\rho)$ satisfies the differential equation

$$\rho^2 u_n''(\rho) + \rho u_n'(\rho) + k_0^2\rho^2 u_n(\rho) = \nu_n^2 u_n(\rho) - \frac{j2}{\pi}\rho' \delta(\rho - \rho'). \tag{A3}$$

Applying the second-kind KL transform in Eq. (A3) and observing that $u_n(\rho)$ complies with Eq. (8) with $i=2$, it is extracted

$$\nu^2 \mathrm{KL}_2\{u_n(\rho)\} = \nu_n^2 \mathrm{KL}_2\{u_n(\rho)\} - \frac{j2}{\pi} H^{(2)}_{\nu}(k_0\rho'). \tag{A4}$$

As a consequence,

$$\mathrm{KL}_2\{u_n(\rho)\} = -\frac{j2}{\pi}\frac{H^{(2)}_{\nu}(k_0\rho')}{\nu^2 - \nu_n^2} \tag{A5}$$

and

$$\mathrm{KL}_2\{u(\rho)\} = \frac{1}{\pi - \varphi_0} H^{(2)}_{\nu}(k_0\rho') \sum_{n=0}^{\infty} \frac{\varepsilon_n}{\nu^2 - \nu_n^2} \cos[\nu_n(\varphi - \varphi')]. \tag{A6}$$

The above equation can be further simplified via

$$\begin{aligned} \frac{\cos[\nu(\varphi_0 - \pi + |\varphi - \varphi'|)]}{\sin[\nu(\pi - \varphi_0)]} &= \frac{2\nu}{\pi - \varphi_0} \sum_{n=0}^{\infty} \frac{\varepsilon_n}{\nu^2 - \nu_n^2} \\ &\quad \times \cos[\nu_n(\varphi - \varphi')], \end{aligned} \tag{A7}$$

which is based on the fact that the function on the left-hand side of Eq. (A7) is meromorphic with respect to ν.[32] So,

$$\mathrm{KL}_2\{u(\rho)\} = \frac{H^{(2)}_{\nu}(k_0\rho')}{2\nu} \frac{\cos[\nu(\varphi_0 - \pi + |\varphi - \varphi'|)]}{\sin[\nu(\pi - \varphi_0)]}, \tag{A8}$$

which, for $\varphi = \varphi_3$, is the operand of Eq. (44).

Pertaining to the calculation of $\mathrm{KL}_1\{u_n(\rho)\}$ and successively of $\mathrm{KL}_1\{u(\rho)\}$, we have taken into account that

$$\begin{aligned} &\sqrt{\frac{2}{\pi k_0}} \lim_{\rho \to \infty} \sqrt{x}[u_n'(\rho) - jk_0 u_n(\rho)] e^{j(k_0\rho - 1/2\nu\pi - 1/4\pi)} \\ &= -\frac{j4}{\pi} e^{j\nu_n\pi/2} J_{\nu_n}(k_0\rho') e^{-j\nu\pi/2}. \end{aligned} \tag{A9}$$

Then, application of the first-kind KL transform on Eq. (A3) yields

$$\begin{aligned} &\nu^2 \mathrm{KL}_1\{u_n(\rho)\} - \frac{j4}{\pi} e^{j\nu_n\pi/2} J_{\nu_n}(k_0\rho') e^{-j\nu\pi/2} \\ &= \nu_n^2 \mathrm{KL}_1\{u_n(\rho)\} - \frac{j2}{\pi} H^{(1)}_{\nu}(k_0\rho') \end{aligned} \tag{A10}$$

or equivalently

$$\mathrm{KL}_1\{u_n(\rho)\} = \frac{j4}{\pi} e^{j\nu_n\pi/2} J_{\nu_n}(k_0\rho') \frac{e^{-j\nu\pi/2}}{\nu^2 - \nu_n^2} - \frac{j2}{\pi} \frac{H^{(1)}_{\nu}(k_0\rho')}{\nu^2 - \nu_n^2} \tag{A11}$$

and

$$\begin{aligned} \mathrm{KL}_1\{u(\rho)\} &= \frac{1}{\pi - \varphi_0} H^{(1)}_{\nu}(k_0\rho') \sum_{n=0}^{\infty} \frac{\varepsilon_n}{\nu^2 - \nu_n^2} \cos[\nu_n(\varphi - \varphi')] \\ &\quad - \frac{2}{\pi - \varphi_0} \sum_{n=0}^{\infty} \varepsilon_n e^{j\nu_n\pi/2} J_{\nu_n}(k_0\rho') \frac{e^{-j\nu\pi/2}}{\nu^2 - \nu_n^2} \\ &\quad \times \cos[\nu_n(\varphi - \varphi')]. \end{aligned} \tag{A12}$$

Finally, through the utilization of Eq. (A7) in Eq. (A12), it is retrieved

$$\begin{aligned} \mathrm{KL}_1\{u(\rho)\} &= \frac{H^{(1)}_{\nu}(k_0\rho')}{2\nu} \frac{\cos[\nu(\varphi_0 - \pi + |\varphi - \varphi'|)]}{\sin[\nu(\pi - \varphi_0)]} \\ &\quad - \frac{2}{\pi - \varphi_0} \sum_{n=0}^{\infty} \varepsilon_n e^{j\nu_n\pi/2} J_{\nu_n}(k_0\rho') \frac{e^{-j\nu\pi/2}}{\nu^2 - \nu_n^2} \\ &\quad \times \cos[\nu_n(\varphi - \varphi')]. \end{aligned} \tag{A13}$$

---

*tsibukis@auth.gr

[1] V. G. Veselago, Sov. Phys. Usp. **10**, 509 (1968).

[2] G. V. Eleftheriades and K. G. Balmain, *Negative-Refraction Metamaterials* (John Wiley & Sons, Hoboken, NJ, 2005).

[3] C. Caloz and T. Itoh, *Electromagnetic Metamaterials: Transmission Line Theory and Microwave Applications: The Engineering Approach* (John Wiley & Sons, Hoboken, NJ, 2006).

[4] N. Engheta and R. W. Ziolkowski, *Metamaterials: Physics and Engineering Explorations* (IEEE, Piscataway, NJ, 2006).

[5] R. Marqués, F. Martín, and M. Sorolla, *Metamaterials with Negative Parameters: Theory, Design and Microwave Applications* (John Wiley & Sons, Hoboken, NJ, 2008).

[6] A. Alù and N. Engheta, Phys. Rev. B **75**, 024304 (2007).

[7] T. F. Gundogdu, N. Katsarakis, M. Kafesaki, R. S. Penciu, G.

Konstantinidis, A. Kostopoulos, E. N. Economou, and C. M. Soukoulis, Opt. Express **16**, 9173 (2008).

[8] D. R. Smith, W. J. Padilla, D. C. Vier, S. C. Nemat-Nasser, and S. Schultz, Phys. Rev. Lett. **84**, 4184 (2000).

[9] D. R. Smith, S. Schultz, P. Markos, and C. M. Soukoulis, Phys. Rev. B **65**, 195104 (2002).

[10] X. Chen, T. M. Grzegorczyk, B. I. Wu, J. Pacheco, Jr., and J. A. Kong, Phys. Rev. E **70**, 016608 (2004).

[11] M. G. Silveirinha, Phys. Rev. B **75**, 115104 (2007).

[12] C. R. Simovski and S. A. Tretyakov, Phys. Rev. B **75**, 195111 (2007).

[13] J. B. Pendry, Phys. Rev. Lett. **85**, 3966 (2000).

[14] R. Ruppin, J. Phys.: Condens. Matter **13**, 1811 (2001).

[15] D. L. Sounas, N. V. Kantartzis, and T. D. Tsiboukis, Phys. Rev. E **76**, 046606 (2007).

[16] J. B. Pendry and S. A. Ramakrishna, J. Phys.: Condens. Matter **15**, 6345 (2003).

[17] L. B. Felsen and N. Marcuvitz, *Radiation and Scattering of Waves* (IEEE, Piscataway, NJ, 1994).

[18] E. Marx, IEEE Trans. Antennas Propag. **41**, 1001 (1993).

[19] J. Meixner, IEEE Trans. Antennas Propag. **20**, 442 (1972).

[20] A. A. Sukhorukov, I. V. Shadrivov, and Y. S. Kivshar, Int. J. Numer. Model. **19**, 105 (2006).

[21] H. Wallén, H. Kettunen, and A. Sihvola, Metamaterials **2**, 113 (2008).

[22] L. Knockaert, F. Olyslager, and D. De Zutter, IEEE Trans. Antennas Propag. **45**, 1374 (1997).

[23] V. Daniele and P. Uslenghi, Radio Sci. **42**, RS6S31 (2007).

[24] C. Monzon, D. W. Forester, and P. Loschialpo, Phys. Rev. E **72**, 056606 (2005).

[25] C. Monzon, D. W. Forester, and R. Burkhart, Phys. Rev. E **73**, 036620 (2006).

[26] V. G. Daniele and P. L. E. Uslenghi, Proceedings of International Conference on *Electromagnetics in Advanced Applications*, (Turin, Italy, 2007), p. 68–70.

[27] A. Taflove and S. C. Hagness, *Computational Electrodynamics: The Finite-Difference Time-Domain Method*, 3rd ed. (Artech House, Norwood, MA, 2005).

[28] R. W. Ziolkowski and E. Heyman, Phys. Rev. E **64**, 056625 (2001).

[29] Y. Zhao, P. Belov, and Y. Hao, Phys. Rev. E **75**, 037602 (2007).

[30] M. I. Stockman, Phys. Rev. Lett. **98**, 177404 (2007).

[31] D. S. Jones, J. Inst. Math. Appl. **26**, 133 (1980).

[32] P. M. C. Morse and H. Feshbach, *Methods of Theoretical Physics, Part 1* (McGraw-Hill, New York, 1953).

[33] For example, if $\mu_r = -1 - j0.01$ and $\varphi_0 = 30°$, $\nu_p = \pm(10.12 - j3)$ for even modes and $\nu_p = \pm(10.12 + j3)$ for odd ones.